

Biomimetic Localized Gel Electrolyte
Biomimetic Localized Gel Electrolyte for Practical Zinc Anode

Yibo Zhu, Shengyong Gao,* Shuangbin Zhang, Yang Chen, Peng Liu, Haotian Meng, Zhiruo Luo, Xuan Chen, Zhenhai Wen, Lina Wang,* Lianzhou Wang, Bin Luo,* and Jisheng Zhou*

Abstract: Incompatible electrode/electrolyte interface often leads to dendrite growth, parasitic reactions, and corrosion, posing significant challenges to the application of Zn anodes. Herein, we introduce a biomimetic antifreeze protein localized gel electrolyte (ALGE) with multifunctional capabilities to address these issues by combining electrolyte modification with interface optimization. ALGE modifies the Zn^{2+} solvation structure and the hydrogen-bond network adjacent to the zinc anode, effectively suppressing hydrogen evolution. Additionally, ALGE promotes (002)_{Zn} crystal plane-dominated deposition by protein-zinc surface interactions, enabling a long-range dendrite-free deposition. The absence of by-products and inhibited corrosion further highlights the practical potential of ALGE. Symmetric cells with ALGE-modified zinc demonstrate an impressive lifespan of 610 h under a current density of 10 mA cm⁻² and a capacity of 10 mAh cm⁻². The pouch cell integrating a manganese dioxide cathode and ALGE-modified Zn anode retains 75.8% of its capacity after 200 cycles at 1 A g⁻¹. This localized gel electrolyte strategy offers a practical and scalable approach to stabilizing Zn anodes for next-generation energy storage systems.

Introduction

Rechargeable Zn-based aqueous batteries (ZABs) emerge as a potential candidate for the storage and conversion of renewable energy resources, encouraged by the intrinsic merits of Zn, low redox potential (−0.76 V vs standard hydrogen electrode), high theoretical capacity (820 mA h g⁻¹), and the non-negligible cost and safety advantages.^[1–4] However, the practical application of ZABs is hindered by challenges including low coulombic efficiency (CE) and limited cycle lifespan.^[5,6] These issues primarily stem from the incompatible anode-electrolyte interface, which leads to hydrogen evolution reactions (HER), zinc corrosion, and dendrite growth.^[7,8]

The construction of hydrogel electrolyte is an efficient way to stabilize the Zn anode but faces the limitation of low ionic conductivity.^[9] Among various strategies proposed for modifying the anode-electrolyte interface or restructuring the electrolyte structure, gelation stands out for its ability to achieve multiple benefits synchronously, making it a promising method for achieving homogenous Zn deposition without HER and corrosion.^[10–13] However, the low ionic conductivity of hydrogel electrolyte, resulting from the increased ion transport barrier, diminishes the performance of ZABs, undermining the potential advantages of this approach.^[14,15] Fortunately, the challenge of low ionic conductivity in hydrogel electrolytes can be addressed through confinement strategy.^[16] By creating a localized interfacial gel layer, rather

[*] Y. Zhu, Y. Chen, P. Liu, H. Meng, X. Chen, J. Zhou
 State Key Laboratory of Chemical Resource Engineering, Beijing Key Laboratory of Electrochemical Process and Technology for Materials Technology, National Engineering Research Center for Fuel Cell and Hydrogen Source, Beijing University of Chemical Technology, Beijing 100029, P.R. China

E-mail: zhousj@mail.buct.edu.cn

S. Gao, S. Zhang, Z. Luo, L. Wang, B. Luo
 Australia Institute for Bioengineering and Nanotechnology (AIBN), The University of Queensland, Brisbane, QLD 4072, Australia

E-mail: shengyong.gao@uq.edu.au
 b.luo1@uq.edu.au

Z. Wen, L. Wang
 State Key Laboratory of Structural Chemistry, and Fujian Provincial Key Laboratory of Materials and Techniques toward Hydrogen Energy, Fujian Institute of Research on the Structure of Matter, Chinese Academy of Sciences, Fujian 350002, P.R. China
 E-mail: wanglina@fjirm.ac.cn

Z. Wen, L. Wang
 Fujian Science & Technology Innovation Laboratory for Optoelectronic Information of China, Fuzhou, Fujian 350108, P.R. China

L. Wang
 Fujian Key Laboratory of Green Extraction and High-Value Utilization of New Energy Metals, Fuzhou University, Fuzhou, P.R. China

L. Wang
 School of Chemical Engineering, The University of Queensland, Brisbane, QLD 4072, Australia

Additional supporting information can be found online in the Supporting Information section

© 2025 The Author(s). Angewandte Chemie International Edition published by Wiley-VCH GmbH. This is an open access article under the terms of the [Creative Commons Attribution-NonCommercial License](#), which permits use, distribution and reproduction in any medium, provided the original work is properly cited and is not used for commercial purposes.

than using bulk gel electrolytes, the diffusion resistance of zinc ions away from the gel interface can be minimized, significantly improving ion transport without compromising the electrolyte's performance.^[17]

The unclear working principles of interfacial gelation led to ambiguous design concepts. For bulk gel electrolyte, the key working principles involve tailoring the solvation shell to create a nonwater-dominated structure.^[18,19] For the interface modification, the vital design concept is improving interface compatibility.^[20,21] However, the interfacial gelation integrates the characteristic of bulk electrolyte and interface, i.e., it changes the local electrolyte structure only adjacent to the electrode/electrolyte interface.^[22,23] Its complex working mechanism combines the reconstruction of Zn^{2+} solvation structure,^[17] the evolution of the H-bond network,^[24] the interface interactions between Zn^{2+} , H_2O , gel-network, and zinc anode.^[21] The adjustment of different interactions can cause different electrolyte-function improvements.^[25] Constructing a localized gel electrolyte that meets the requirements of dendrite-free, HER-free, and corrosion-free requires a comprehensive and clear design principle.^[26] Neglecting any aspect of the effective mechanisms can cause the interface-functional loss and leak to battery failure, and further, a misunderstanding of the true working mechanism behind interfacial gelation.

Biomimetic design ignites the hope of establishing a robust multifunctional gel layer on zinc anode, providing an opportunity to better understand the working principles of interfacial gelation.^[17,20,21] Antifreeze proteins (AFP), found in organisms inhabiting low-temperature environments, perform effectively in the perturbation of long-range water dynamics.^[27,28] As proposed, the formation of water bridges on the surface of AFPs causes disorder in the H-bond network in the first solvation shell, which propagates to the remaining solvation shells at low temperatures, leading to a depressed freezing point to facilitate the long-term survival of organisms in the cold environment.^[29–31] Given their ability to interfere with the H-bonding structure, we consider AFPs to be “high-quality candidates” for creating a gel interface on zinc anode. Thus, reconstructing the local electrolyte structure by an AFP layer has the potential to rebuild the Zn solvation shell, limit the movement of active water molecules, and optimize the zinc deposition behavior.

In this study, we report a multifunctional biomimetic AFP membrane as a localized gel electrolyte on the Zn anode to rebuild the local electrolyte structure adjacent to the anode. The AFP localized gel electrolyte (ALGE) effectively inhibits the HER, dendrite growth, and zinc corrosion synchronously. Its working principles mirror that of bulk gel electrolyte but are confined to the anode-electrolyte interface, avoiding a significant drop in ionic conductivity. On the one hand, the ALGE changes the solvation structure of Zn^{2+} adjacent to the anode, turning the $\text{Zn}(\text{H}_2\text{O})_6^{2+}$ to $\text{Zn}(\text{H}_2\text{O})_4^{2+}$ while reconstructing the tetrahedral H-bond network to a linear configuration. The polarization of Zn^{2+} on H_2O molecules is weakened, and the anchoring effect of AFP on H_2O molecules reduces the free water content, thus undercutting the HER tendency. On the other hand, during Zn^{2+} passing through the interface, the ALGE regulates ion

flux, eliminating the tip effect and guiding uniform current distribution. This leads to planner Zn deposition dominated by (002) crystal plane. Symmetric cells with ALGE-modified Zn electrodes demonstrate excellent durability (610 h) at an ultra-high current density of 10 mA cm^{-2} and a high deposition capacity of 10 mAh cm^{-2} . Full batteries coupled with MnO_2 cathode and ALGE-modified Zn anode show a high-capacity retention of 79.8% after 1500 cycles at 1 A g^{-1} .

Results and Discussion

Attracted by the hydrogen bond restructuring capability, AFP was selected as the matrix of localized gel electrolyte. Its molecular structure and secondary protein structure are shown in Figures S1 and S2, together with the corresponding NMR spectrum (Figure S3). The weight average molecular mass of the AFP is approximately $8.0 \times 10^5 \text{ g mol}^{-1}$ (Figure S4). After being mixed with a 10% mass fraction of polyvinylidene fluoride (PVDF), the AFP was coated on the Zn foil and coagulated into a gel, and further dried to form films, referred as AFP film. In the water-based zinc battery system, the AFP films adsorb the electrolyte (2 M ZnSO_4), transforming into a hydrogel that allows the electrolyte molecules to pass through, thus named as ALGE. The ALGE-modified Cu and Zn electrodes are denoted as ALGE@Cu and ALGE@Zn, respectively. As shown in Figure 1a, ALGE only changes the local electrolyte environment adjacent to the zinc foil without affecting the bulk electrolyte, thus overcoming the low ionic conductivity issue of gel electrolytes by employing a confinement strategy (Figure S5).

ALGE maintains stability in the electrolyte and performs multiple functions during zinc plating and stripping, including inhibiting HER, eliminating dendrites, and alleviating corrosion (Figure 1a). The prepared AFP film appears as a white solid membrane in an anhydrous state (Figure S6). It can adsorb the electrolyte and maintain condensation during electrolyte immersion (Figure S7). The AFP film coated on a zinc foil presents a homogenous film morphology with intimate interface adhesion, which was observed by scanning electron microscopy (SEM) and corresponding energy-dispersive X-ray spectroscopy (EDS) mappings (Figures S8 and S9). After being coated on Zn and soaked in electrolyte, ALGE exhibits multifunctional characteristics: i) ALGE@Zn performs significant corrosion resistance. As indicated by the Tafel curves (Figure 1b), the corrosion potential of the ALGE@Zn electrode ($-0.928 \text{ V vs Ag/AgCl}$) was considerably higher than that of the bare zinc anode ($-0.962 \text{ V vs Ag/AgCl}$). Furthermore, the corrosion current of the ALGE@Zn electrode (0.12 mA cm^{-2}) was significantly reduced compared to the bare zinc anode (2.24 mA cm^{-2}). These results demonstrate a substantially slower corrosion rate for the ALGE@Zn electrode.^[32] This is further supported by the corrosion morphology (Figure S10), where ALGE@Zn presents a smooth surface after soaking in 2 M ZnSO_4 for 96 h, in contrast to the byproducts observed on the bare zinc surface.^[33] X-ray photoelectron spectroscopy (XPS) was used to explore the corrosion products (Figures S11 and S12). With the increase of etching time, the dominant peak in high-resolution Zn

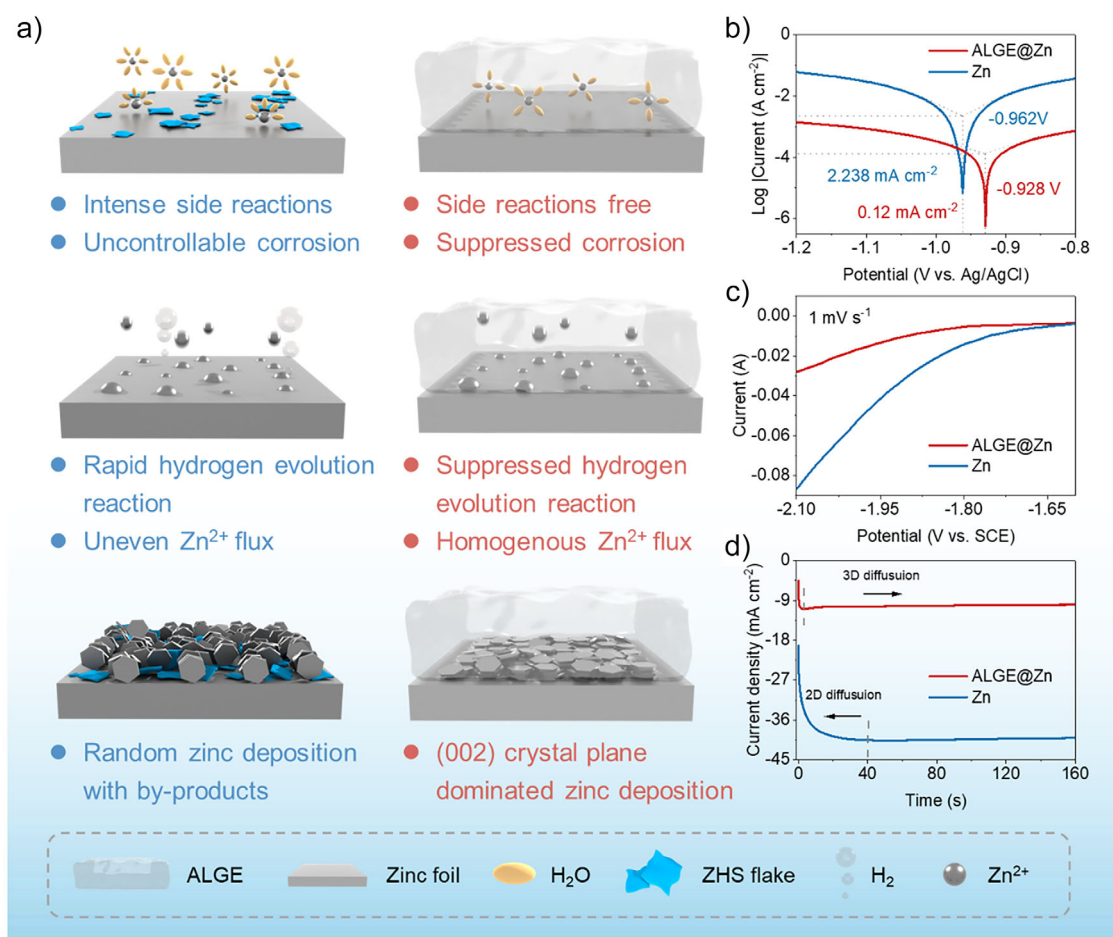


Figure 1. Construction of the multifunctional ALGE toward practical Zn anode. a) Schematic diagrams of the construction and working principle of ALGE-modified Zn anode. b) Tafel curves of Zn foil and ALGE@Zn. c) LSV curves using SCE as the reference electrode in 2 M Na₂SO₄ solution. d) CA curves of Zn||Zn or ALGE@Zn||ALGE@Zn symmetric cells under a constant voltage of -100 mV.

2p XPS of the corroded bare zinc shows a significant shift, indicating a change in the surface zinc's valence state (Zn²⁺) compared to the bulk phase (Zn⁰).^[34] However, the Zn 2p XPS spectra of the ALGE@Zn consistently showed Zn in the zero-valent state. The spectra of other elements also bear this out, confirming the effective inhibition of corrosion reactions by ALGE. ii) The ALGE@Zn electrode exhibits an extended electrochemical window with a higher HER overpotential in linear sweep voltammetry (LSV) curves (Figure 1c), -2.03 V (vs SCE), compared to -1.84 V for bare zinc, indicating suppressed HER.^[35] iii) ALGE accelerates the 3D zinc diffusion process while inhibiting the 2D nucleation, as shown in chronoamperometry (CA, Figure 1d), and thus promotes stable Zn deposition. In contrast, the bare zinc anode undergoes a slower 2D growth process, characterized by a gradual increase in the current over 30 s, indicating the zinc deposition at this stage is uncontrollable and prone to form irregular dendrites.^[36] Cyclic voltammetry (CV) was also conducted to investigate the nucleation and growth processes of the zinc deposition (Figure S13). Additional active zinc exposure reflects the interfacial stability of ALGE@Zn. For bare zinc, a smaller enclosed area suggests fewer nucleation sites, confirming a tardy deposition process.^[37]

ALGE acts as a thin layer of hydrogel electrolyte, allowing aqueous electrolyte to pass through and changing the solvation shell of Zn²⁺ adjacent to the electrode. The fluorescence luminescence technique provided crucial evidence of zinc deposition beneath the ALGE. After different plating/stripping cycles, the ALGE@Zn was dyed by fluorescein isothiocyanate (FITC) to visualize the distribution of the AFP molecule. The strong fluorescence in Figure 2a indicates the protein exists on the top of deposited Zn constantly.

As a comparison, bare Zn after cycling and dying still present as dark under the fluorescence microscope (Figure S14). SEM images provide further confirmation that Zn²⁺ deposits on the zinc foil after passing through the ALGE instead of depositing inside or on the top of ALGE. After plating 2 mA h cm⁻² of zinc, the zinc elements can only be found beneath ALGE, as shown in both top-view (Figure 2b) and the side-view (Figure S15). Figure 2c illustrates the zinc deposition process, highlighting the changes in the Zn²⁺ solvation structure, which was primarily revealed by high-resolution mass spectrometry (HR-MS) in positive ion mode (Figure 2d). The ionic cluster of Zn²⁺ in ALGE transitions from the three typical clusters with a certain mass/charge

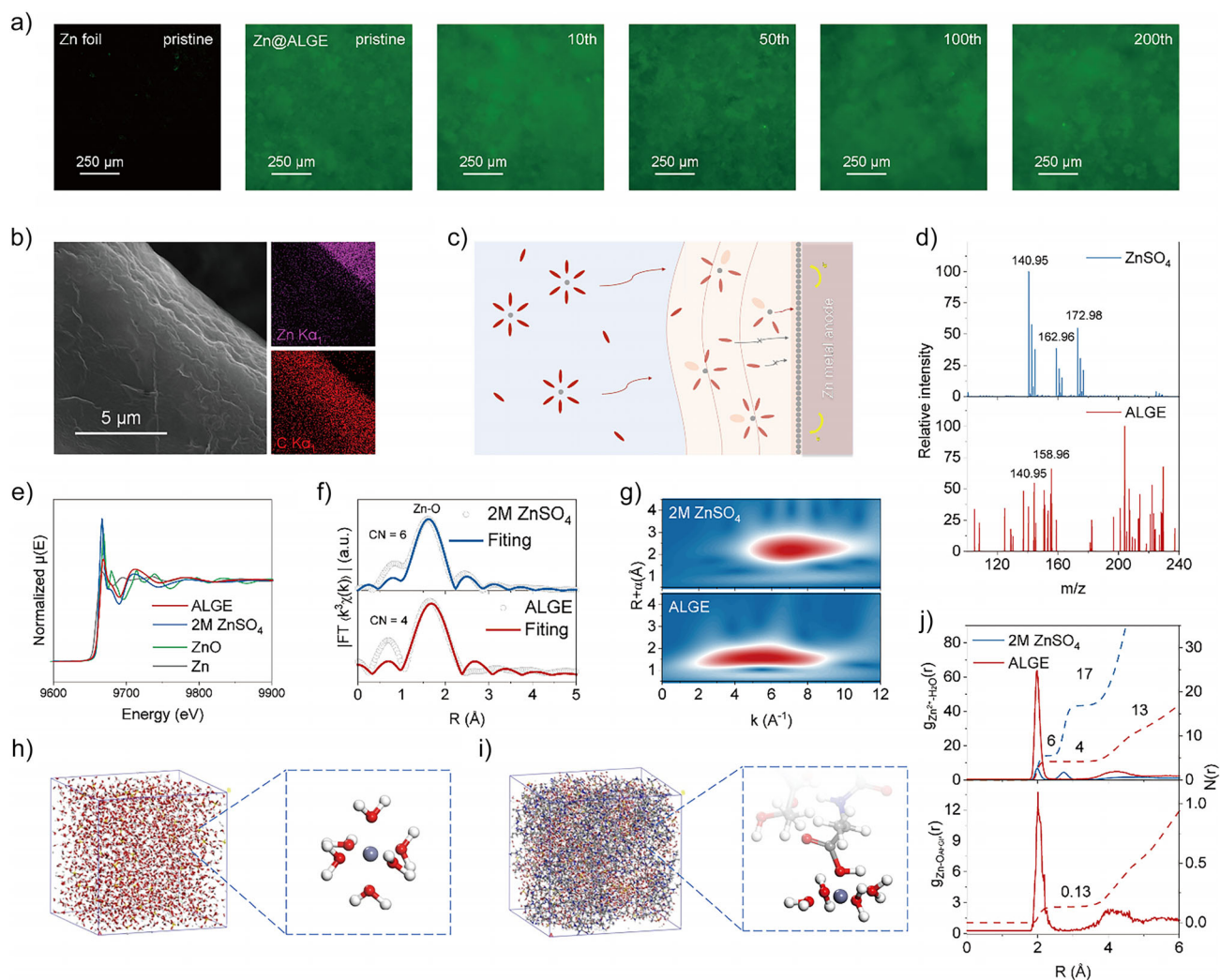


Figure 2. Solvation structure of Zn^{2+} . a) Fluorescence microscope images of the Zn electrodes after different plating/stripping cycles at the current density of 1 mA cm^{-2} and the deposition capacity of 1 mA h cm^{-2} . b) A SEM top view image of ALGE@Zn after zinc deposition (2 mA h cm^{-2}) with corresponding EDS mapping of Zn and C elements. c) Schematic illustration of the working mechanism of ALGE. d) High-resolution mass spectra of 2 M ZnSO_4 and ALGE in the positive-ion mode. e–g) Zn K-edge XANES, k₃-weighted FT-EXAFS, WT-EXAFS contour plots of 2 M ZnSO_4 and ALGE. h,i) Snapshot of the MD simulation results for the Zn^{2+} solvation shell of 2 M ZnSO_4 and ALGE with representative solvation structure. j) RDF of Zn^{2+} obtained from MD simulation results.

ratio in 2 M ZnSO_4 to the ionic fragments with a broad mass/charge ratio distribution, which indicates alterations in the Zn^{2+} solvation structure and its interactions with AFP and water molecules.^[38] In negative ion mode, ZnSO_4 electrolyte shows a similar spectrum with that of ALGE, indicating the weak interactions between SO_4^{2-} and other particles (Figure S16). X-ray absorption near-edge structure (XANES) provides detailed information of the solvation structure, where ALGE exhibits a different Zn-K adsorption edge compared with ZnSO_4 electrolyte (Figures 2e and S17), indicating a change in the valence state of Zn aroused from different coordination structure.^[39] By fitting the dominant peak of Fourier-transform (FT) k₃-weighted EXAFS spectra (Figure S18) in both k-space (Figures 2f and S19) and R-space (Figure S20) using the least squares method, the Zn-O coordination number ($\text{CN}_{\text{Zn-O}}$) was obtained. Compared with the number of 2 M ZnSO_4 ($\text{CN}_{\text{Zn-O}} = 6$), the Zn-O

coordination number in ALGE decreased to 4, indicating the first solvent shell of Zn change from the $\text{Zn}^{2+}-(\text{H}_2\text{O})_6$ in 2 M ZnSO_4 to $\text{Zn}^{2+}-(\text{H}_2\text{O})_4$ in ALGE.^[40] Furthermore, the wavelet-transform-EXAFS (WT-EXAFS) plot further distinguishes the local coordination environment (Figures 2g and S21), where the maximum intensities of the Zn-O present a significant shift in ALGE compared with that in 2 M ZnSO_4 .^[41] Molecular dynamics (MD) simulations were used to further investigate the migration of the solvation structure of Zn^{2+} (Figure 2h,i). The radial distribution functions (RDFs, Figure 2j) show that, in 2 M ZnSO_4 electrolyte, Zn^{2+} preferentially coordinates with six H_2O molecules to form a primary solvation structure, while for the ALGE, the Zn^{2+} solvation shell is significantly different from that of ZnSO_4 , showcasing the decrease of $\text{CN}_{\text{Zn-O}}$ from 6 to 4, consisting of the EXAFS fitting results. In short, during the Zn^{2+} migration from aqueous ZnSO_4 electrolyte to ALGE, its solvation

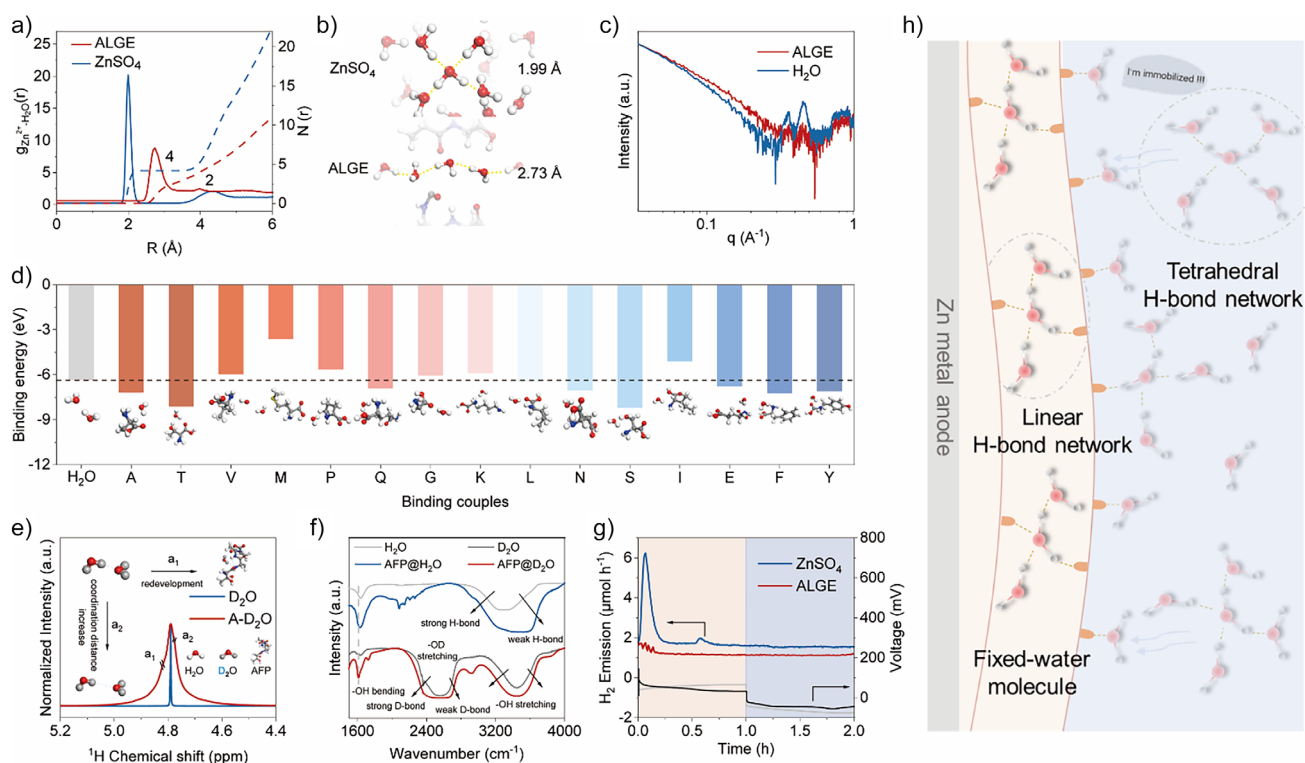


Figure 3. Interactions between AFP and water molecules and the H-bond network evolution. a) The $\text{O}_{\text{H}_2\text{O}}-\text{O}_{\text{H}_2\text{O}}$ RDFs and on the same scale, integrated coordination numbers of 2 M ZnSO_4 and ALGE obtained from MD simulation results. b) Schematic diagram of the H-bond network structure in 2 M ZnSO_4 and ALGE. c) SAXS of pure H_2O and the AFP film after absorbing water. d) Binding energies between different monomers of AFP with water molecules. e) ^1H NMR spectra of D_2O compared with that of AFP film that has absorbed D_2O . f) FT-IR spectra of D_2O , and H_2O compared with that of AFP film after absorbing D_2O or H_2O . g) In situ DEMS toward the H_2 evolution of $\text{Zn}||\text{Zn}$ and $\text{ALGE}@Zn||\text{ALGE}@Zn$ symmetric cells. h) Schematic diagram of the H-bond network evolution.

structure undergoes a dramatic transformation. The H_2O molecules coordinated with Zn^{2+} are partly removed, which relieves the polarization of Zn^{2+} on H_2O molecules and thus weakens the HER tendency.

ALGE reconstructs the H-bond network adjacent to the Zn anode and thus inhibits HER. Compared with the tetrahedral H-bond network in 2 M ZnSO_4 electrolyte (Figure 3a), the H-bond network in ALGE turns to a linear structure (Figure 3b), indicating a weaker $\text{H}_2\text{O}-\text{H}_2\text{O}$ interaction. The strong AFP- H_2O interaction is the reason for the H-bond network migration, which was primarily explored by small angle X-ray scattering (SAXS) where the water clusters in pure water present as two dominant peaks in $0.3-0.5 \text{ \AA}^{-1}$ region, while the intensity of these two peaks significantly decreases for AFP that have absorbed water (Figure 3c), indicating the disruption of water-water H-bond network.^[42] The reason for the disruption of $\text{H}_2\text{O}-\text{H}_2\text{O}$ interaction is the AFP can form a stronger H-bond with water, which can be first revealed by thermogravimetric (TG, Figure S22). Because of the AFP- H_2O interaction, water molecules are anchored around the protein molecules, thus exhibiting stronger thermal stability and less weight loss. To further ascertain the origin of strong protein-water interaction, density functional theory (DFT) calculations were performed to determine the binding energies between water molecules and different monomers of AFP (Figure 3d). The calculation results indicate that most

components of AFP have a stronger binding affinity to water molecules compared with the $\text{H}_2\text{O}-\text{H}_2\text{O}$ interaction.

The strength of H-bonds was revealed by nuclear magnetic resonance (NMR). As shown in Figure S23, the dominant peak of ^1H NMR spectra of ALGE appears at around 4.8 ppm, which is higher than that of ZnSO_4 , 4.3 ppm, indicating a stronger H-bond in ALGE.^[43] However, it is hard to distinguish which specific interaction contributes to the enhanced H-bond. Thus, AFP was mixed with D_2O to further explore the protein-water interaction. For D_2O , its main peak appears at 4.79 ppm, but for AFP, an additional shoulder peak at a higher chemical shift, 4.82 ppm occurs, which is aroused from the AFP- D_2O interaction with a higher strength. Fourier transform infrared spectroscopy (FT-IR) and Raman spectroscopy (Raman) give similar results (Figure 3f and Figures S24 and S25). Compared with the ZnSO_4 electrolyte, in both H_2O and D_2O , ALGE forms a stronger H-bond and causes the red shift of the -OH stretching adsorption peak. At the same time, $\text{H}_2\text{O}-\text{H}_2\text{O}$ interactions are weakened, introducing the blue shift of the -OH stretching peak. Strong protein- H_2O interaction and weaker $\text{H}_2\text{O}-\text{H}_2\text{O}$ interaction jointly contribute to the significantly wider peak corresponding to the -OH group.^[44] As a consequence, as illustrated in Figure 3h, AFP regulates the Zn^{2+} solvation shell and disrupts the H-bond network among water molecules, significantly reducing the amount

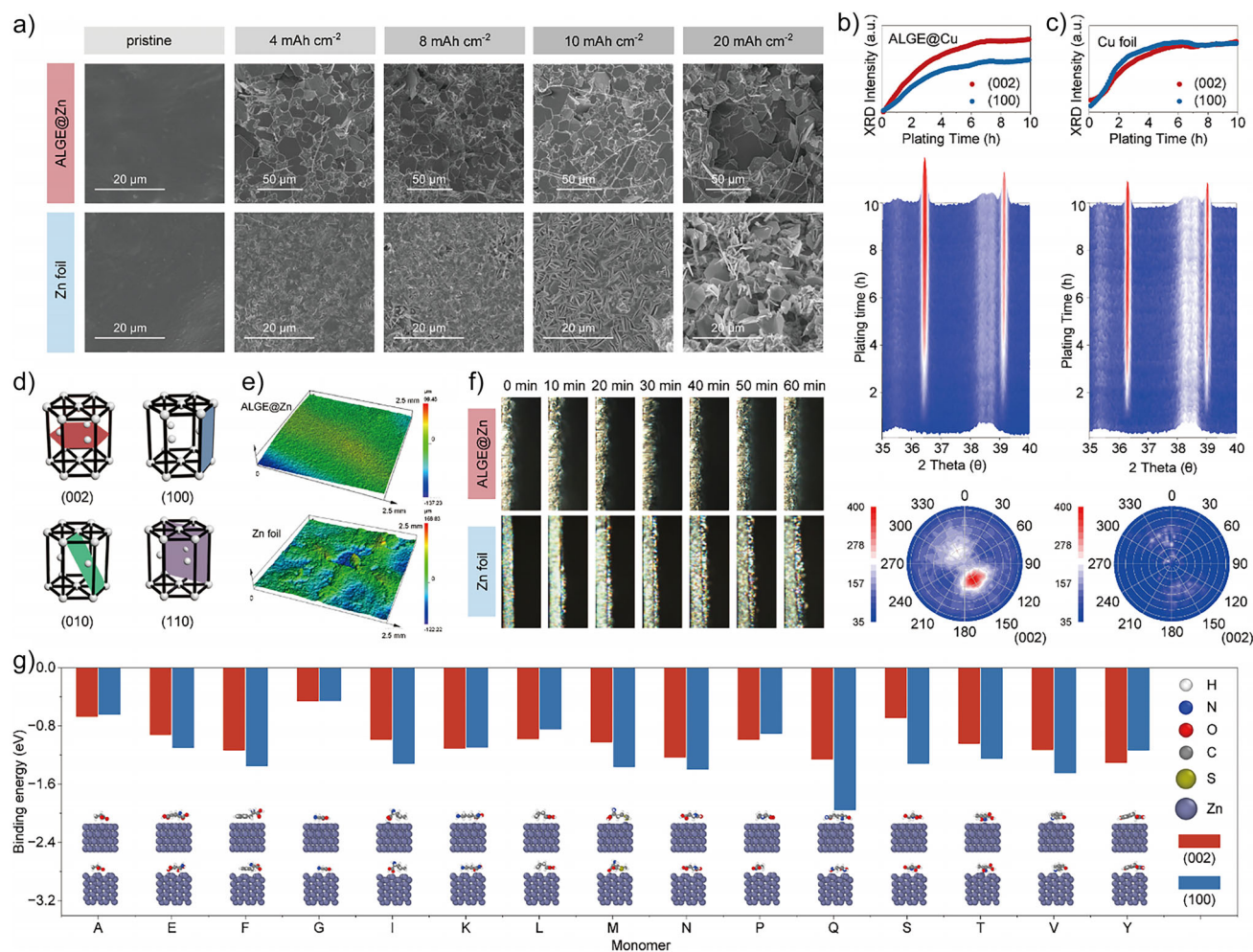


Figure 4. Electrochemical growth pattern of Zn with multiscale deposition morphology. a) SEM images of Zn foil and ALGE@Zn with different deposition capacity. b, c) In situ XRD patterns of the Zn^{2+} electroplating process on ALGE@Cu and Cu foil under the current density of 2 mA h cm^{-2} together with the intensity profile of (002) and (100) crystal plane, and X-ray diffraction pole figures of deposited Zn (2 mA h cm^{-2}) on ALGE@Cu and Cu foil. d) Schematic diagram of various crystallographic orientations of Zn. e) LCSM images of Zn plated (2 mA h cm^{-2}) on ALGE@Zn and Zn foil. f) In situ optical microscope of the Zn^{2+} electroplating process on ALGE@Zn and Zn foil under the current density of 2 mA h cm^{-2} . g) Binding energies and corresponding structures of different protein monomers on Zn (002) and Zn (100).

of active water reaching the zinc anode and resulting in a weakened HER. In situ electrochemical mass spectrometry (DEMS) demonstrates the hydrogen emission (Figure 3g), where the symmetric cell with ALGE@Zn electrodes presents a significantly declined hydrogen emission compared with the battery with pure Zn electrode, providing practical evidence for the inhibited HER.

Encouraged by the interactions between AFPs and zinc surface, ALGE shows the ability to guide the byproduct-free (002) dominated planner deposition. The Zn deposition morphology with different capacities was directly visualized by SEM (Figure 4a). On ALGE@Zn, the electroplated Zn shows a 2D growth morphology, the deposited zinc is parallel to the original substrate, manifested as a typical hexagonal lattice corresponding to (002) crystal plane of Zn that fills the field of view.^[45] As a comparison, the zinc deposition morphology on bare zinc foil exhibits a disordered growth with a large amount of acicular by-products.^[46] Under the atomic force microscope (AFM), the

hexagonal close-packed deposited Zn on ALGE@Zn was directly visualized (Figures S26A and S27A), corresponding to a homogenous roughness (Figure S28A). However, on bare Zn foil, the random zinc deposition was observed with significant fluctuation of roughness (Figures S26B–S28B).

In situ XRD gives a deep insight into the electrochemical growth pattern of Zn on Cu substrate. The Zn deposition presents as a random process on Cu foil, showcasing a growth of each crystal plane (Figure 4c), where a synchronous growth of the diffraction intensity of (002) and (100) crystal plane and the nondominant texture of deposited Zn reflected in the X-ray diffraction pole figures was observed. However, for ALGE@Cu, the Zn plating is oriented, where the (002) plane presents as a prior orientation with the fast rise of the intensity of XRD (Figure 4b) and the concentrated (002) diffraction intensity in the X-ray diffraction pole figures is also significant. Furthermore, after long-cycle repeated electroplating and stripping, the XRD patterns of bare Zn and ALGE@Zn electrodes were recorded (Figure S29). Interestingly, after

cycling, the Zn crystal texture of ALGE@Zn was significantly different from the original ALGE@Zn, presenting as (002) plane dominated (Figure S29A). As a comparison, the deposited Zn on bare Zn foil presents as a random texture (Figure S29B), which could be reflected by the peak intensity ratio of (002) over (100), showcasing the increase from 0.809 to 6.25 of ALGE@Zn (Figure S30) compared with that of bare Zn foil with a slight change. The peak intensity ratios of (002) over (101) and (002) over (102) also show similar trends (Figure S30). The (002)_{Zn} plane dominant deposition emphasizes a reliable ordered planar Zn plating/stripping. Because, on the one hand, the (002)_{Zn} plane is predominantly parallel to the basal crystal of the electrode.^[47] On the other hand, a lower thermodynamic free energy is associated with the exposed closest-packed plane (002) in hexagonal close-packed (hcp) metals, which can inhibit the parasitic reactions.^[48]

The prevention of parasitic reactions by ALGE was reflected by the by-product-free deposition process. After depositing 2 mA h cm⁻² of Zn, the thin sheets corresponding to the typical characteristic of basic zinc sulfate (Zn₄SO₄(OH)₆•5H₂O) was observed on Zn anode under SEM (Figures S31 and S32), consisting with the XRD testing results (Figure S33).^[49] XPS provides the detailed chemical composition of the Zn-anode surface (Figure S34). Plated Zn on ALGE@Zn is more inclined to zinc metal. However, for zinc foil, the binding energy of deposited Zn is more inclined to the Zn-O configuration, which is manifested as the by-products. XANES in fluorescence mode (Figure S35) provides further confirmation of the Zn species, where cycled Zn exhibits a different Zn-K edge compared with the original Zn foil, indicating a higher valence close to ZnO. The similar adsorption edge of ALGE@Zn and Zn reference indicates the dominance of Zn⁰. The k₃-weighted FT-EXAFS of ALGE@Zn and Zn in R-space (Figures S36 and S37) and k-space (Figure S38) emphasize the existence of the Zn-O coordination on the surface of cycled Zn anode. This can be directly visualized by WT-EXAFS analysis (Figure S39) where the maximum corresponding to Zn-O coordination on ALGE@Zn is relatively weak. As a final confirmation, high-resolution transmission electron microscopy (HRTEM) together with selected area electron diffraction (SAED) was used to observe the anode surface after the cycle, the obvious compact lattice was observed on ALGE@Zn with distinct diffraction spots on the selected electron diffraction pattern (Figure S40), compared with the thick by-product layer on pure Zn foil with diffraction rings. Thus, ALGE prevents Zn from suffering from the generation of by-products with poor conductivity, which can cause charge accumulation and irregular dendrites growth.

The (002)_{Zn} plane-dominated deposition process contributes to a homogenous deposition morphology. As shown in laser confocal scanning microscopy (LCSM, Figure 4e), uniform Zn deposition was observed on ALGE@Zn, compared with that of Zn foil with a drastic fluctuation in surface height. In situ optical microscopy also recorded the Zn nucleation and subsequent deposition process. During galvanostatic deposition (2 mA cm⁻²) on the Zn foil, several individual Zn nuclei appeared after 30 min, corresponding

to the inhomogeneous and scanty Zn nucleation. After 40 min of plating, these unevenly distributed nuclei evolve into Zn dendrites. Conversely, with the increase of deposition capacity, the deposited layer gradually thickens on the ALGE@Zn, and no obvious Zn dendrites were found on the electrode surface, which is attributed to the more intensive and finer Zn nucleus seeds and uniform subsequent deposition (Figure 4f). First-principle calculations based on density functional theory give the reason for the (002)_{Zn} plane-dominated deposition process. It was revealed that the overall monomers preferentially bind to the Zn (100) surface over the Zn (002) surface, exhibiting the strongest binding energies of -1.95 and -1.31 eV for monomer Q and Y on the Zn (100) and Zn (002) surfaces, respectively (Figure 4g). The strong binding of the monomer to the Zn (100) surface hinders charge transfer and Zn²⁺ deposition, suppressing nucleation and growth in the vertical direction. This promotes the growth of the low-energy (002) plane, which typically grows more slowly, leading to a deposition mode dominated by the (002) plane.

Contributed from the HER-free, by-products-free, and ALGE-regulated Zn deposition, the electrochemical activity of ALGE@Zn anode is uniform and intense, which was directly visualized by scanning electrochemical cell microscopy (SECCM) synchronously with topography.^[50] For bare Zn anode, the Zn deposition topographical is uneven (Figures 5a and S41A), consisting of the previous evidence, more importantly, its active surface can be passivated by insulated by-products, bubbles generated by HER, resulting in a low current response (Figures 5c and S41B).^[51] The topography of the ALGE@Zn substrate is a homogeneous surface without obvious fluctuation (Figures 5b and S41C). Due to the absence of insulation by-products and hydrogen bubbles on the surface, the uniform current distribution indicates an active surface of the entire electrode of ALGE@Zn (Figures 5d and S41D). From the aspect of electric field distributions, which was stimulated by COMSOL Multiphysics, as depicted in Figure S42, due to the reconstruction of the local electrolyte environment by ALGE on Cu foil, the electric field on ALGE@Cu is more uniform than that of bare Zn, which eliminates the tip effect. Homogenous electric field and current distribution jointly contribute to a uniform Zn²⁺ flux, which was revealed by an electron probe X-ray micro-analyzer (EPMA). For ALGE@Zn, the even ion flux (Figure 5e) on the electrode surface ultimately presents a nonaggregated ion distribution. However, on Zn foil, significant fluctuations of Zn²⁺ ions distribution were detected, further confirming the existence of the tip effect.^[52] As a result, local electrolyte structure modification disperses the current and electric field distribution and thus eliminates the tip effect during zinc deposition, contributing a practical zinc anode.

The ALGE modification significantly improved the electrochemical performance of the zinc anode. To evaluate the reversibility of Zn deposition/stripping, asymmetric Zn||Cu cells were first assembled (Figure 6a). The nucleation overpotential of Zn on ALGE@Cu is 41 mV (Figure 6b), indicating a lower deposition barrier. At a current density of 1 mA cm⁻² and a deposition capacity of 1 mA h cm⁻², the

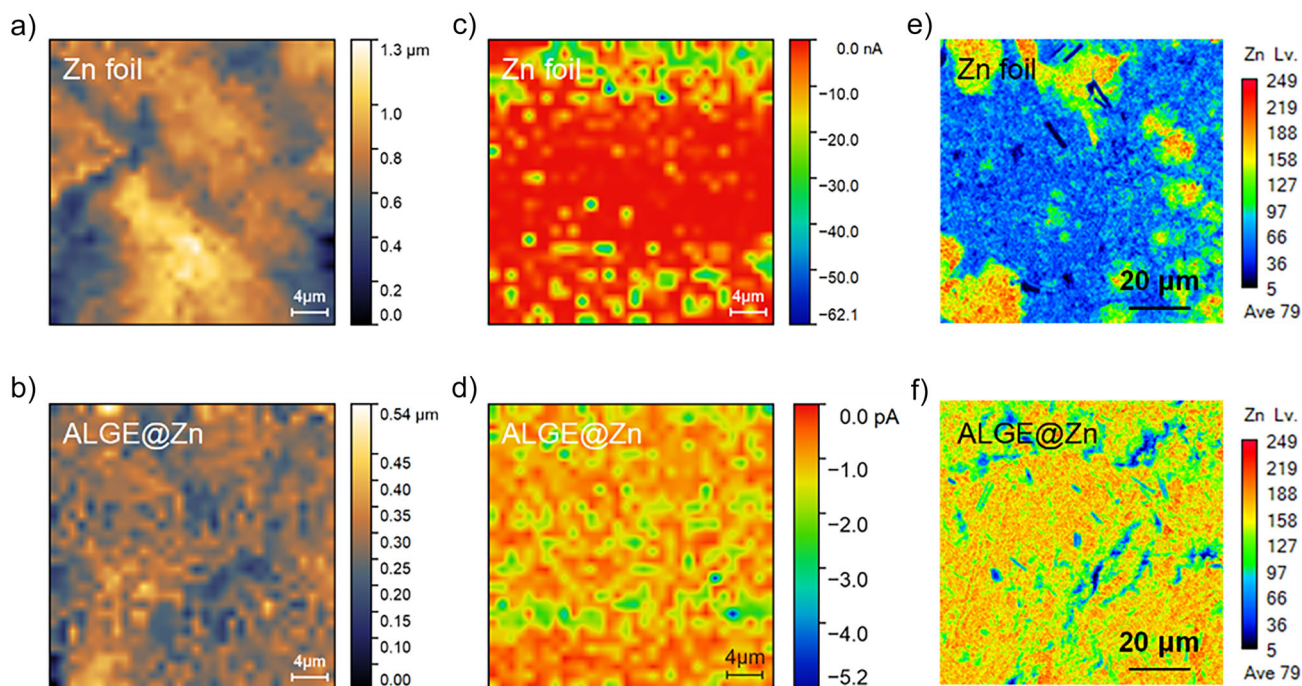


Figure 5. Topography and current activity of Zn and ALGE@Zn electrode. a,b) SECCM topographical image (pixel: 32×32) of Zn and ALGE@Zn. c,d) Electrochemical activity images ($E_{app} = -1$ V) of this area. e,f) EPMA images of Zn plated (2 mA h cm^{-2}) on ALGE@Zn and Zn foil.

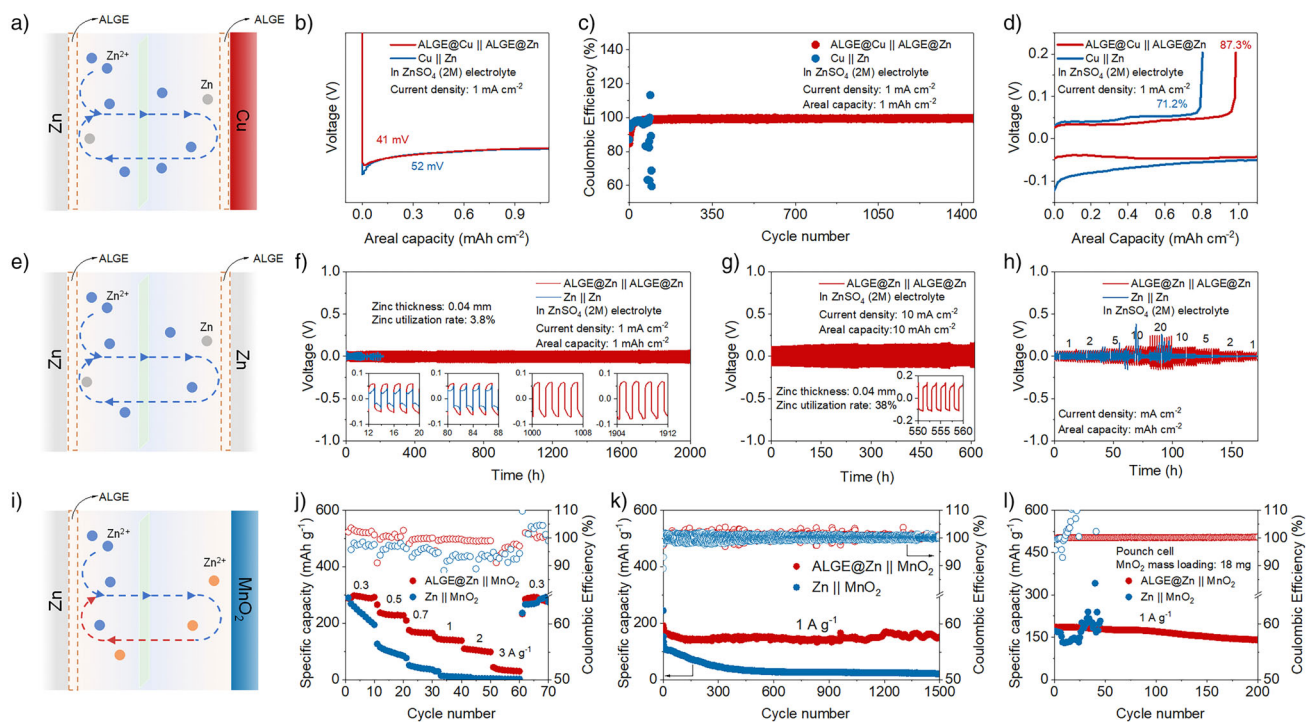


Figure 6. Electrochemical performance of half, symmetric, and full cells. a) Schematic diagram of the working principle of ALGE in half batteries. b) Zn nucleation overpotential at 1 mA cm^{-2} . c) CE of the half cells under the current density of 1 mA cm^{-2} with the deposition capacity of 1 mA h cm^{-2} of ALGE@Zn||Cu and Zn||Cu half cells d) Corresponding charge/discharge profiles. e) Schematic illustration of the working principle of ALGE in symmetric cells. f) Cycling performance of ALGE@Zn||ALGE@Zn and Zn||Zn symmetric cells at 1 mA cm^{-2} with the areal capacity of 1 mA h cm^{-2} g) Cycling performance of ALGE@Zn||ALGE@Zn and Zn||Zn symmetric cells at 10 mA cm^{-2} with the areal capacity of 10 mA h cm^{-2} . h) Rate performance of ALGE@Zn||ALGE@Zn and Zn||Zn symmetric cells. i) Schematic diagram of the working principle of ALGE in full batteries. j) Rate performance and k) cycling performance of full batteries. l) Cycling performance of the pouch cells under 1 A g^{-1} .

Zn||Cu half-cell without ALGE rapidly degraded in the initial 50 cycles, with an extremely unstable CE. In contrast, the cell with ALGE-modified Cu and Zn maintains a stable and high CE (99%) for over 1400 cycles. The corresponding magnified voltage curves (Figure S43) of the ALGE@Zn||ALGE@Cu cell exhibit moderate voltage fluctuations during Zn plating/stripping, highlighting the effectiveness of ALGE modification. In contrast, the Zn||Cu half-cell shows significant voltage instability, indicating an uneven Zn deposition process. This superior stability (Figure 6c) and higher CE (Figure 6d) highlight the reduced side reactions, controlled nucleation, and reversible zinc deposition enabled by ALGE. Comparing the performance of half cells between ALGE and other electrodes reported in previous works, the performance of ALGE@Zn is still impressive, indicating the practical performance of ALGE@Zn anode (Table S3).

To further assess the stability of ALGE during Zn deposition and stripping, we extracted ALGE from ALGE@Zn||ALGE@Cu cells at different charge/discharge states. These cells were cycled at a current density of 3 mA cm^{-2} and a deposition capacity of 3 mA h cm^{-2} . The FT-IR and Raman spectra of ALGE remain largely unchanged throughout the Zn deposition/stripping process, indicating that the C–C backbone and hydrogen-bond network remained stable during zinc migration and reaction (Figures S44A and S44B). Additionally, the morphology of ALGE shows no significant changes, further confirming its structural integrity and physical stability (Figure S44C).

Symmetric batteries were assembled to explore the cycling stability of the ALGE@Zn electrode (Figure 6e). Under 1 mA cm^{-2} and 1 mA h cm^{-2} , the ALGE@Zn||ALGE@Zn cell exhibits an expanded cycle life of 2000 h with a stable polarization voltage, significantly outperforming the Zn||Zn cells, which lasted only 150 h (Figure 6f). Under a higher current density (2 mA cm^{-2}) and (2 mA h cm^{-2}), the ALGE@Zn electrodes again showed superior performance, achieving stable cycling for 1300 h (Figure S45). Remarkably, even at an impressive high current density of 10 mA h cm^{-2} and a deposition capacity of 10 mA h cm^{-2} , ALGE@Zn||ALGE@Zn symmetric cells maintained an ultra-long lifespan of 610 h with a low overpotential of 200 mV (Figure 6g). The thickness of the zinc foil used in coin cells is 0.04 mm, and the zinc utilization rate under the deposition capacity of 10 mA h cm^{-2} is calculated to be 38%. When compared with recent reports (Table S4), ALGE@Zn shows a balance between cycle life and zinc utilization rate. Electrochemical impedance spectroscopy was used to reveal the absence of a soft short circuit (Figure S47).^[53] The Zn||Zn cell shows a significant decrease in impedance after a dramatic raise, indicative of dendrite penetration through the separator with the by-products accumulation, while the ALGE@Zn||ALGE@Zn cells exhibited a stable impedance after cycling, confirming their stable operation. The rate performance of ALGE cells was evaluated across a range of current densities from 1 to 20 mA cm^{-2} , and the results show that the zinc plating/stripping reversibility of ALGE@Zn electrode is significantly better than that of bare zinc (Figure 6h). Compared with the zinc anode reported recently (Table S5 and Figure S46)^[54–61] the superior perfor-

mance of ALGE@Zn remains impressive. This is attributed to the enhanced nucleation and growth kinetics, highlighting the practical potential of the ALGE@Zn anode.

The outstanding plating/stripping performance of ALGE-modified Zn anode underscores its practical application potential. Full batteries were assembled using ALGE@Zn as the anode and MnO_2 as the cathode (Figure 6i and Figures S48 and S49). The ALGE@Zn|| MnO_2 full cells deliver a high average reversible specific capacity of $305.9 \text{ mA h g}^{-1}$ at 0.3 A g^{-1} with an average CE of 99.4% at various rates (Figure 6j). The overall mass-energy density and volume energy density were calculated as 113.5 Wh kg^{-1} and 467.2 Wh L^{-1} . Even at a current density of 1 A g^{-1} , the ALGE@Zn|| MnO_2 full cell remains a high reversible capacity of $186.6 \text{ mA h g}^{-1}$ and maintained 79.8% of its capacity after 1500 cycles, in contrast to the significant capacity decrease of the Zn|| MnO_2 full cell (Figure 6k). The charge–discharge curves provide detailed insights into the charge/discharge process, where the full battery using ALGE@Zn anode presented a splendid capacity rendition. From the second to the tenth cycle, the curves show better overlap (Figure S50), indicating high reversibility during early cycles. In CV curves of full battery with ALGE@Zn anode (Figure S51), prominent reduction peaks appear at 1.25 and 1.37 V, corresponding to the intercalation reactions of Zn^{2+} into MnO_2 , accompanied by the reduction of Mn^{4+} to Mn^{2+} . An oxidation peak at 1.58 V corresponds to the reversible extraction of Zn^{2+} from MnO_2 and the oxidation of Mn^{2+} to Mn^{4+} .^[62] In contrast, the CV curves of cells with Zn anode show smaller oxidation and reduction peaks, indicating less Zn^{2+} intercalation and extraction. Pouch cells were further assembled with MnO_2 cathodes to evaluate the practical performance of the ALGE@Zn anode. At 1 A g^{-1} (Figure 6l), the ALGE@Zn|| MnO_2 pouch cell delivers a high reversible capacity of $186.7 \text{ mA h g}^{-1}$ and retains 75.8% of its capacity after 200 cycles. In contrast, the Zn|| MnO_2 pouch cell experiences rapid capacity decay due to the accumulation of by-products and gas formation. The ALGE@Zn assisted pouch cell also presents excellent capacity retention, with the second to the tenth charge/discharge cycles overlapping well (Figure S52), indicating a highly reversible Zn^{2+} storage process. Compared with recently published zinc anode modification strategies, the practical performance of ALGE@Zn anode is still significant (Table S4). Iodine has been extensively studied as a cathode material in aqueous Zn^{2+} batteries.^[63,64] When paired with an I_2 cathode, ALGE@Zn also demonstrates excellent application potential. The cycling performance and corresponding voltage profiles of the assembled ALGE@Zn|| I_2 pouch cell are shown in Figure S53. Under a current density of 3C (following precycling at 0.5 C), the ALGE@Zn|| I_2 cell maintains stable cycling over 104 cycles, with a high-capacity retention of 95.7%. In contrast, the bare Zn|| I_2 pouch cell exhibits a significant capacity decline after the first five cycles, indicating poor cycling stability. In short, the outstanding electroplating/stripping reversibility, cycling stability, and high-capacity retention in half-cell, symmetrical cells, and full batteries with ALGE@Zn anodes collectively demonstrate that the biomimetic AFP-based localized gelation strategy is an effective and practical approach for practical zinc anode modification.

Conclusion

In summary, we have designed a biomimetic localized gel electrolyte that combines the benefits of electrolyte modification and interface optimization, effectively addressing critical issues associated with dendrite growth, HER, and zinc corrosion for zinc anode. The strong interactions between AFPs and water reorganize the H-bond network adjacent to the zinc anode, turning the solvation structure of Zn^{2+} from $Zn(H_2O)_6^{2+}$ to $Zn(H_2O)_4^{2+}$ during passing through the ALGE, thereby inhibiting the HER. Moreover, ALGE preferentially combines on the (100)_{Zn} crystal plane, exposing the (002)_{Zn} plane for uniform, dendrite-free Zn deposition without by-products or corrosion. As a result, ALGE@Zn enables the symmetrical batteries to achieve an expanded lifespan of up to 2000 h at 1 mA cm⁻² and 1 mA h cm⁻², and can even withstand a high current density of 10 mA cm⁻² and a high areal capacity of 10 mA h cm⁻² for 610 h. Integrating the MnO₂ cathode and ALGE@Zn anode, the pouch cell demonstrates considerable practical potential, retaining a capacity of over 141 mA h g⁻¹ after 200 cycles. This work proposed a confinement strategy to construct a localized gel electrolyte to synchronously achieve HER-free, dendrite-free, and corrosion-free zinc deposition, providing a promising Zn anode for practical application.

Acknowledgements

This work was supported by the National Natural Science Foundation of China (52173244 and 51872019), the Postdoctoral Fellowship Program of CPSF, China (GZB20230758), Fujian Key Laboratory of Green Extraction and High-value Utilization of New Energy Metals (2023-KFKT-2) and China Postdoctoral Science Foundation (2024M753237). The authors are grateful for the financial support of the Australian Research Council through its Future Fellowship (FT200100279), and Discovery Programs. The authors appreciate the 1W1B-XAFS Station of Beijing Synchrotron Radiation Facility (BSRF) and the Medium Energy X-ray Absorption Spectroscopy MEX-2 beamline of Australian Synchrotron (part of ANSTO) for their support. The authors thank Eaglenos Sciences, Inc., CHINA for the help with the SECCM experiments. The authors extend their gratitude from Shiyanjia Lab for providing assistance with the fluorescence microscope. All first-principles calculations were carried out on the Taiyi cluster supported by the Center for Computational Science and Engineering of Southern University of Science and Technology. The authors also thank the scientific and technical support from the Australian Microscopy & Microanalysis Research Facility at the Centre for Microscopy and Microanalysis, the University of Queensland and the Queensland node of the Australian National Fabrication Facility, a company established under the National Collaborative Research Infrastructure Strategy to provide nano and microfabrication facilities for Australia's researchers. S. G. and S. Z. are supported by China Scholarship Council.

Open access publishing facilitated by The University of Queensland, as part of the Wiley - The University of Queens-

land agreement via the Council of Australian University Librarians.

Conflict of Interests

The authors declare no conflict of interest.

Data Availability Statement

The data that support the findings of this study are available from the corresponding author upon reasonable request.

Keywords: Hydrogen bond network • Interfacial gelation • Localized gel electrolyte • Solvation structure • Zinc anode

- [1] J. Zheng, Q. Zhao, T. Tang, J. Yin, C. D. Quilty, G. D. Renderos, X. Liu, Y. Deng, L. Wang, D. C. Bock, *Science* **2019**, *366*, 645–648.
- [2] L. Cao, D. Li, T. Pollard, T. Deng, B. Zhang, C. Yang, L. Chen, J. Vatamanu, E. Hu, M. J. Hourwitz, *Nat. Nanotechnol.* **2021**, *16*, 902–910.
- [3] Y. Liang, H. Dong, D. Aurbach, Y. Yao, *Nat. Energy* **2020**, *5*, 646–656.
- [4] S. W. D. Gourley, R. Brown, B. D. Adams, D. Higgins, *Joule* **2023**, *7*, 1415–1436.
- [5] C. Li, S. Jin, L. A. Archer, L. F. Nazar, *Joule* **2022**, *6*, 1733–1738.
- [6] L. Cao, D. Li, E. Hu, J. Xu, T. Deng, L. Ma, Y. Wang, X.-Q. Yang, C. Wang, *J. Am. Chem. Soc.* **2020**, *142*, 21404–21409.
- [7] Y. Zhu, G. Liang, X. Cui, X. Liu, H. Zhong, C. Zhi, Y. Yang, *Energy Environ. Sci.* **2024**, *17*, 369–385.
- [8] J. Cao, D. Zhang, X. Zhang, Z. Zeng, J. Qin, Y. Huang, *Energy Environ. Sci.* **2022**, *15*, 499–528.
- [9] Y. Wang, Q. Li, H. Hong, S. Yang, R. Zhang, X. Wang, X. Jin, B. Xiong, S. Bai, C. Zhi, *Nat. Commun.* **2023**, *14*, 3890.
- [10] Q. He, Y. Zhong, J. Li, S. Chai, Y. Yang, S. Liang, Z. Chang, G. Fang, A. Pan, *Adv. Energy Mater.* **2024**, *14*, 2400170.
- [11] H. Lu, J. Hu, X. Wei, K. Zhang, X. Xiao, J. Zhao, Q. Hu, J. Yu, G. Zhou, B. Xu, *Nat. Commun.* **2023**, *14*, 4435.
- [12] G. Li, Z. Zhao, S. Zhang, L. Sun, M. Li, J. A. Yuwono, J. Mao, J. Hao, J. Vongsivut, L. Xing, *Nat. Commun.* **2023**, *14*, 6526.
- [13] F. Wang, J. Zhang, H. Lu, H. Zhu, Z. Chen, L. Wang, J. Yu, C. You, W. Li, J. Song, *Nat. Commun.* **2023**, *14*, 4211.
- [14] K. Zhu, J. Luo, D. Zhang, N. Wang, S. Pan, S. Zhou, Z. Zhang, G. Guo, P. Yang, Y. Fan, *Adv. Mater.* **2024**, *36*, 2311082.
- [15] R. Qi, W. Tang, Y. Shi, K. Teng, Y. Deng, L. Zhang, J. Zhang, R. Liu, *Adv. Funct. Mater.* **2023**, *33*, 2306052.
- [16] S. Zhang, H. Ao, J. Dong, D. Wang, C. Wang, X. Xu, Z. Hou, J. Yang, *Angew. Chem. Int. Ed.* **2025**, *64*, e202414702.
- [17] W. Guo, L. Xu, Y. Su, Z. Tian, C. Qiao, Y. Zou, Z. Chen, X. Yang, T. Cheng, J. Sun, *ACS Nano* **2024**, *18*, 10642–10652.
- [18] H. Ge, X. Xie, X. Xie, B. Zhang, S. Li, S. Liang, B. Lu, J. Zhou, *Energy Environ. Sci.* **2024**, *17*, 3270–3306.
- [19] X. Zhou, Y. Zhou, L. Yu, L. Qi, K.-S. Oh, P. Hu, S.-Y. Lee, C. Chen, *Chem. Soc. Rev.* **2024**, *53*, 5291–5337.
- [20] S. J. Zhang, J. Hao, H. Wu, Q. Chen, C. Ye, S. Z. Qiao, *Adv. Mater.* **2024**, *36*, 2404011.
- [21] J. Huang, Y. Zhong, H. Fu, Y. Zhao, S. Li, Y. Xie, H. Zhang, B. Lu, L. Chen, S. Liang, *Adv. Mater.* **2024**, *36*, 2406257.
- [22] Z. Shi, Z. Xu, Z. Liu, Y. Ren, L. Zhang, J. Ren, S. Chen, T. Liu, *Adv. Funct. Mater.* **2024**, *35*, 2414451.

- [23] Z. Meng, Y. Jiao, P. Wu, *Angew. Chem. Int. Ed.* **2023**, *135*, e202307271.
- [24] T. Qiu, T. Wang, W. Tang, Y. Li, Y. Li, X. Lang, Q. Jiang, H. Tan, *Angew. Chem. Int. Ed.* **2023**, *135*, e202312020.
- [25] S. Chen, M. Zhang, P. Zou, B. Sun, S. Tao, *Energy Environ. Sci.* **2022**, *15*, 1805–1839.
- [26] J. Wei, P. Zhang, J. Sun, Y. Liu, F. Li, H. Xu, R. Ye, Z. Tie, L. Sun, Z. Jin, *Chem. Soc. Rev.* **2024**, *53*, 10335–10369.
- [27] T. Sun, F.-H. Lin, R. L. Campbell, J. S. Allingham, P. L. Davies, *Science* **2014**, *343*, 795–798.
- [28] A. U. Thosar, Y. Shalom, I. Braslavsky, R. Drori, A. J. Patel, *J. Am. Chem. Soc.* **2023**, *145*, 17597–17602.
- [29] S. S. Mallajosyula, K. Vanommeslaeghe, A. D. MacKerell Jr, *J. Phys. Chem. B* **2014**, *118*, 11696–11706.
- [30] S. Ebbinghaus, K. Meister, B. Born, A. L. DeVries, M. Gruebele, M. Havenith, *J. Am. Chem. Soc.* **2010**, *132*, 12210–12211.
- [31] W. Zhang, H. Liu, H. Fu, X. Shao, W. Cai, *J. Phys. Chem. B* **2022**, *126*, 10637–10645.
- [32] T. Li, S. Hu, C. Wang, D. Wang, M. Xu, C. Chang, X. Xu, C. Han, *Angew. Chem. Int. Ed.* **2023**, *62*, e202314883.
- [33] S. D. Pu, B. Hu, Z. Li, Y. Yuan, C. Gong, Z. Ning, C. Chau, S. Yang, S. Zhang, L. Pi, *Joule* **2023**, *7*, 366–379.
- [34] Z. Cai, J. Wang, Y. Sun, *eScience* **2023**, *3*, 100093.
- [35] Q. Meng, Q. Bai, R. Zhao, P. Cao, G. Zhang, J. Wang, F. Su, X. Zhou, J. Yang, J. Tang, *Adv. Energy Mater.* **2023**, *13*, 2302828.
- [36] Z. Hu, Z. Song, Z. Huang, S. Tao, B. Song, Z. Cao, X. Hu, J. Wu, F. Li, W. Deng, *Angew. Chem. Int. Ed.* **2023**, *135*, e202309601.
- [37] X. Cai, X. Wang, Z. Bie, Z. Jiao, Y. Li, W. Yan, H. J. Fan, W. Song, *Adv. Mater.* **2024**, *36*, 2306734.
- [38] P. Zou, R. Lin, T. P. Pollard, L. Yao, E. Hu, R. Zhang, Y. He, C. Wang, W. C. West, L. Ma, *Nano Lett.* **2022**, *22*, 7535–7544.
- [39] Q. Zhang, Y. Ma, Y. Lu, Y. Ni, L. Lin, Z. Hao, Z. Yan, Q. Zhao, J. Chen, *J. Am. Chem. Soc.* **2022**, *144*, 18435–18443.
- [40] Q. Zhang, Y. Ma, Y. Lu, X. Zhou, L. Lin, L. Li, Z. Yan, Q. Zhao, K. Zhang, J. Chen, *Angew. Chem. Int. Ed.* **2021**, *133*, 23545–23552.
- [41] D. Wang, R. Li, J. Dong, Z. Bai, N. Wang, S. X. Dou, J. Yang, *Angew. Chem. Int. Ed.* **2025**, *64*, e202414117.
- [42] N. Dubouis, A. Serva, R. Berthin, G. Jeanmairet, B. Porcheron, E. Salager, M. Salanne, A. Grimaud, *Nat. Catal.* **2020**, *3*, 656–663.
- [43] R. J. Gomes, R. Kumar, H. Fejzić, B. Sarkar, I. Roy, C. V. Amanchukwu, *Nat. Catal.* **2024**, *7*, 689–701.
- [44] X. Yu, M. Chen, Z. Li, X. Tan, H. Zhang, J. Wang, Y. Tang, J. Xu, W. Yin, Y. Yang, *J. Am. Chem. Soc.* **2024**, *146*(25), 17103–17113.
- [45] Z. Zheng, X. Zhong, Q. Zhang, M. Zhang, L. Dai, X. Xiao, J. Xu, M. Jiao, B. Wang, H. Li, *Nat. Commun* **2024**, *15*, 753.
- [46] X. Yu, Z. Li, X. Wu, H. Zhang, Q. Zhao, H. Liang, H. Wang, D. Chao, F. Wang, Y. Qiao, *Joule* **2023**, *7*, 1145–1175.
- [47] C. Fan, W. Meng, J. Han, T. Li, D. Zuo, S. Deng, D. Li, L. Jiang, *Energy Stor. Mater* **2024**, *71*, 103554.
- [48] Y. Qin, H. Li, C. Han, F. Mo, X. Wang, *Adv. Mater.* **2022**, *34*, 2207118.
- [49] H. Yu, D. Chen, X. Ni, P. Qing, C. Yan, W. Wei, J. Ma, X. Ji, Y. Chen, L. Chen, *Energy Environ. Sci.* **2023**, *16*, 2684–2695.
- [50] J. T. Simon, V. Šedajová, D. Tripathy, H. Smith, S. Clarke, C. P. Grey, S. Menkin, *J. Mater. Chem. A* **2024**, *12*, 24916–24933.
- [51] J. Zhao, Z. Lv, S. Wang, Z. Chen, Z. Meng, G. Li, C. Guo, T. Liu, J. Hui, *Small Methods* **2023**, *7*, 2300731.
- [52] F. Liu, S. Xu, W. Gong, K. Zhao, Z. Wang, J. Luo, C. Li, Y. Sun, P. Xue, C. Wang, *ACS Nano* **2023**, *17*, 18494–18506.
- [53] Q. Li, A. Chen, D. Wang, Z. Pei, C. Zhi, *Joule* **2022**, *6*, 273–279.
- [54] F. Wu, J. Zhang, L. Ma, P. Ruan, Y. Chen, S. Meng, R. Yin, W. Shi, W. Liu, J. Zhou, *Angew. Chem. Int. Ed.* **2024**, e202421787.
- [55] Y. Shen, P. Fu, J. Liu, K. Sun, H. Wen, P. Liu, H. Lv, T. Gu, X. Yang, L. Chen, *Nano Res. Energy* **2024**, *3*, e9120115.
- [56] H. Ren, S. Li, B. Wang, Y. Zhang, T. Wang, Q. Lv, X. Zhang, L. Wang, X. Han, F. Jin, *Adv. Mater.* **2023**, *35*, 2208237.
- [57] X. Guo, H. Hong, Q. Li, J. Zhu, Z. Wu, Y. Wang, S. Yang, Z. Huang, Y. Huang, N. Li, *Matter* **2024**, *7*, 4014–4030.
- [58] M. Qiu, P. Sun, Y. Wang, L. Ma, C. Zhi, W. Mai, *Angew. Chem. Int. Ed.* **2022**, *61*, e202210979.
- [59] B. Liu, C. Wei, Z. Zhu, Y. Fang, Z. Bian, X. Lei, Y. Zhou, C. Tang, Y. Qian, G. Wang, *Angew. Chem. Int. Ed.* **2022**, *134*, e202212780.
- [60] H. Hong, Y. Wang, Y. Zhang, B. Han, Q. Li, X. Guo, Y. Guo, A. Chen, Z. Wei, Z. Huang, *Adv. Mater.* **2024**, *36*, 2407150.
- [61] S. Chen, S. Li, L. Ma, Y. Ying, Z. Wu, H. Huang, C. Zhi, *Angew. Chem. Int. Ed.* **2024**, *63*, e202319125.
- [62] T. M. Narayanan, Y. G. Zhu, E. Gençer, G. McKinley, Y. Shao-Horn, *Joule* **2021**, *5*, 2934–2954.
- [63] S. J. Zhang, J. Hao, H. Wu, Q. Chen, C. Ye, S. Z. Qiao, *Adv. Mater* **2024**, *36*, 2404011.
- [64] Q. Chen, J. Hao, Y. Zhu, S. J. Zhang, P. Zuo, X. Zhao, M. Jaroniec, S. Z. Qiao, *Angew. Chem. Int. Ed.* **2025**, *64*, e202413703.

Manuscript received: January 20, 2025

Revised manuscript received: February 26, 2025

Accepted manuscript online: March 12, 2025

Version of record online: March 22, 2025